

Effects of coflow temperature and composition on ethanol spray flames in hot-diluted coflow

H. Correia Rodrigues, M.J. Tummers, E.H. van Veen, D.J.E.M. Roekaerts*

Department of Process and Energy, Section Fluid Mechanics, Delft University of Technology, Mekelweg 2, 2628 CD Delft, The Netherlands



ARTICLE INFO

Article history:

Available online 5 November 2014

Keywords:

Spray flames
Mild combustion
Hot-diluted coflow
Phase Doppler anemometry
Coherent anti-Stokes Raman scattering
Ethanol fuel

ABSTRACT

Ethanol pressure-swirl sprays issuing in a hot-diluted oxidizer coflow with different temperature and composition were studied. The bulk coflow temperature was varied together with the oxygen volume fraction. The bulk coflow temperature was changed from 1480 K to 1225 K and the oxygen volume fraction from 7.1% to 10.1%. The liquid mass flow rates were chosen to yield spray flames with nearly identical Weber number. Laser Doppler anemometry, phase Doppler anemometry and coherent anti-Stokes Raman scattering were applied in the spray region and the coflow inlet. The current measurements provide a thorough description of the spray structure, droplet dispersion and gas temperature fields as well as a comprehensive database useful for validation of numerical models. Visual observations of the flame luminescence reveal that the lift-off height depends on the liquid mass flow rates as well as the coflow conditions. The lift-off height is shown to increase for lower coflow temperatures and higher liquid mass flow rates. It is found that lift-off behavior depends on the droplet convective, vaporization and chemical time scales prior to ignition. Phase Doppler anemometry results indicate that the droplet mean size and velocity distribution close to the atomizer are not influenced by the coflow conditions. A flame-front develops at the outer region of the spray where a low density of large droplets are present. A significant number of peak temperatures samples above 2000 K is observed at this location. Decrease of the coflow temperature leads to a reduction of the local peak temperatures. Closer to the center axis, the local mixture composition becomes increasingly rich and the heat-release is lower than in the outer region.

© 2014 Elsevier Inc. All rights reserved.

1. Introduction

Moderate or Intense Low-Oxygen Dilution (MILD) combustion has prompted great interest as a new clean combustion concept. The operation principle is based on the dilution of fuel with pre-heated air and high temperature combustion gas recirculation yielding an overall small temperature increase due to the heat capacity augmentation and, consequently, low NO_x emissions (Wünning and Wünning, 1997; Cavalieri and de Joannon, 2004). This unique combustion mode has completely different characteristics from a conventional operating method concerning flammability limits, combustion stability, combustion noise, and ignition process and has been studied both in industrial furnaces and laboratory scale setups for various gaseous fuels. Issues of interest for the studies included flame chemistry (Medwell and Dally, 2012; Medwell et al., 2007; Ihme and See, 2011), flow dynamics (Oldenhof et al., 2011, 2013; Dally et al., 2002), stabilization

mechanisms (Oldenhof et al., 2010), emissions formation and quantification of the thermal field uniformity under various operational conditions (Coelho and Peters, 2001; Veríssimo et al., 2011, 2013).

A review of earlier research show that MILD combustion for liquids fuels has received little attention (Tsuji et al., 2002; Weber et al., 2005; Wu et al., 2007; Derudi and Rota, 2011). Studies have been performed mainly in industrial and semi-industrial scale furnaces and focused on the sustainability of MILD regime for heavy fuel oils as well as the factors resulting in furnace performance deterioration. Tsuji et al. (2002) investigated the applicability of heavy fuel oils in industrial furnaces operating in MILD conditions. The oxygen content and the pre-heated air temperature were varied systematically ($Y_{O_2} = 3\text{--}15\%$ and $T = 573\text{--}1553\text{ K}$) to investigate the changing state of the flame form and the resulting pollutant emission. A strong dependence of the flame stability and chemiluminescence with the preheated air and oxygen dilution was observed as well as a substantial increase of NO_x production for heavy fuel oils. Other studies (Weber et al., 2005; Wu et al., 2007) in industrial scale test furnaces operating in MILD conditions

* Corresponding author. Tel.: +31 15 27 82470; fax: +31 15 27 82838.

E-mail address: D.J.E.M.Roekaerts@tudelft.nl (D.J.E.M. Roekaerts).

showed a homogenized temperature field in furnaces. However, only for certain nozzle configurations and fuel oil grades a high-temperature process without the penalty of increased NO_x emissions was achievable. [Derudi and Rota \(2011\)](#) carried out an experimental study on a dual-nozzle laboratory scale burner arranged in a crossflow configuration. Pure liquid *n*-octane and other mixtures involving hydrocarbons commonly found in practical fuels were used. The experiments were designed to map the dependence of the MILD combustion region with two main operating parameters: average combustion chamber temperature and dilution ratio. Results on NO_x and CO emissions showed that MILD conditions of liquid hydrocarbons was attainable for lower combustion gas recirculation ratio as compared to the LPG fuel counterparts. Additionally, increase of the oxygen dilution was witnessed to have a slight positive effect on pollutant emissions for lower average combustion chamber temperature.

The aforementioned studies clearly show the practical importance of the technology, however, many aspects in the near-injector region are not investigated. In the spray region, the fuel stream first has to be shattered into an ensemble of droplets with a desirable distribution of sizes and velocities in order to achieve the required rate of vaporization, chemical heat-release, levels of conversion and pollutant emissions. Instabilities at the liquid–gas interface in the near-atomizer region lead to primary and secondary break-up. The liquid fragments in surrounding gas form a dispersed multiphase flow, where droplets are evaporating and subject to turbulent dispersion. The dispersed droplets modify the gas-phase turbulence and the released fuel vapor depending on the relative speed of evaporation, mixing and combustion, burns in diffusion flames around individual droplets or clusters of droplets, or in partially premixed gaseous flames ([Jenny et al., 2012](#)). The temperature and composition of the oxidizer influence the time scales of phase change and reaction, making a spray flame in conventional combustion different from that of a hot-diluted combustion regime.

The present work concerns a fundamental experimental study. The objective is to reach understanding of the spray region by using a laboratory scale burner developed to study spray combustion in MILD conditions. The burner design retains the relevant physical processes of practical combustion systems. However, the composition of the gases entrained into the spray are controlled by a secondary burner rather than the furnace aerodynamics. The spray flame is unconfined and specifically designed to allow for easy access of state-of-the-art laser diagnostics ([Barlow, 2007](#)).

[Goix et al. \(1994\)](#), [Cessou and Stepowski \(1996\)](#), and [Stepowski et al. \(1994\)](#) investigated stabilization of flame structures above an airblast injector fed with liquid methanol. The qualitative structure of the reacting spray and its reaction zone were investigated by Mie scattering imaging and OH^* Planar LIF. Phase Doppler anemometry was used to measure droplet size statistics. The results show two outer reaction zones where strong OH signals are present. It is observed that flame stabilization occurs in the large scale mixing structures at the edge of the jet where the small droplets have sufficient time to vaporize, mix with entrained air, and burn. A discussion was presented concerning the lift-off position, motivated by a mixture-fraction formulation. In an effort to establish general features of combusting sprays in hot-diluted coflow without the influence of the near-injector dense region, [O'Loughlin and Masri \(2011\)](#) used a nebuliser instead of a pressure atomizer. Simultaneous high-speed $\text{OH}-\text{CH}^*$ Planar LIF and droplet Mie scattering show that ignition OH kernels formation and growth is the mechanism of spray flame stabilization in hot-diluted conditions. The oxygen mole fraction in the coflow (12% by volume) of [O'Loughlin and Masri \(2011\)](#) is, however, rather high compared to other studies of combustion systems operating in MILD conditions ([Derudi and Rota, 2011](#); [Tsui et al., 2002](#)).

The present study is an extension of earlier work by the authors on the structure of pressure-swirl spray flames in conventional and hot-diluted combustion regime ([Correia Rodrigues et al., 2014](#)). The burner facility, atomizer type and the liquid fuel used in this study were identical. A commercial pressure-swirl atomizer was used for generating the spray. In this way the liquid atomization and gas flow in the combustion chamber are very strongly coupled and experiments remain close to the most common configuration used in industrial practice. All measurements are made up to locations as close to the atomizer as possible to unveil features of the near-injector region. Ethanol was used as fuel because of the well-defined physical properties and well-documented chemical mechanism ([Marinov, 1999](#); [Röhl and Peters, 2009](#)).

In the authors' previous study ([Correia Rodrigues et al., 2014](#)), measurements of profiles of droplet size and velocity and gas-phase temperature were performed in an axisymmetric spray issuing in air and in hot-diluted coflow. The results show that in a reacting spray in air coflow, an inner and an outer flame-front are present. In hot-diluted coflow, weakening of the inner flame-front occurs due to the local gaseous mixture richness. At the location of the outer flame-front temperature samples above 2000 K persist. In this study, three spray issuing in hot-diluted coflows with different temperature and composition were studied. The present study complements our previous work ([Correia Rodrigues et al., 2014](#)) and contributes to the current literature by: (a) describing changes in the flame structure and identifying the driving parameter for peak temperature reduction in the outer flame-front region, (b) providing a comprehensive set of measurements that extend the initial database for model validation of polydisperse sprays, and (c) provide insight into the physical mechanisms controlling the spray flame lift-off height in hot-diluted conditions.

This paper is structured as follows: Section 2 briefly describes the burner facility and measurement techniques used in the present study. Section 3 presents the input parameters as well as the coflow boundary conditions for three test cases. Section 4 presents the results on spray flames visual appearance, lift-off behavior, droplet distribution and spray flame structure. A summary of the spray phenomenology and a discussion of the spray flame stabilization mechanisms is also given. In Section 5, conclusions are presented.

2. Experimental method

2.1. Burner facility

Experiments are carried out in a burner facility ([Fig. 1](#)) at Delft University of Technology. It consists of an ethanol spray ($\text{C}_2\text{H}_5\text{OH}$) issuing in a coflow of hot combustion products. The hot combustion products are generated by a secondary burner. It consists of a hexagonal packing arrangement of identical 5 mm diameter vertical pipes with each end welded to perforated plates. At half-height of each individual vertical pipe, four 0.5 mm holes were drilled in a cross-configuration (see section A-A in [Fig. 1](#)). The incoming air flows through the vertical pipes and mixes with Dutch Natural Gas (DNG) forced through the 0.5 mm holes. The mixture then forms a matrix of small flames stabilized on the perforated plate. A vertical pipe with 270 mm length and 160 mm inner diameter prevents the coflow of hot combustion products from mixing with the surrounding air. As the hot combustion products flow through the vertical pipe their temperature is decreasing due to the heat loss to the surroundings by radiation from the vertical pipe. Hereafter, the coflow of hot combustion products will be referred as 'hot-diluted coflow'.

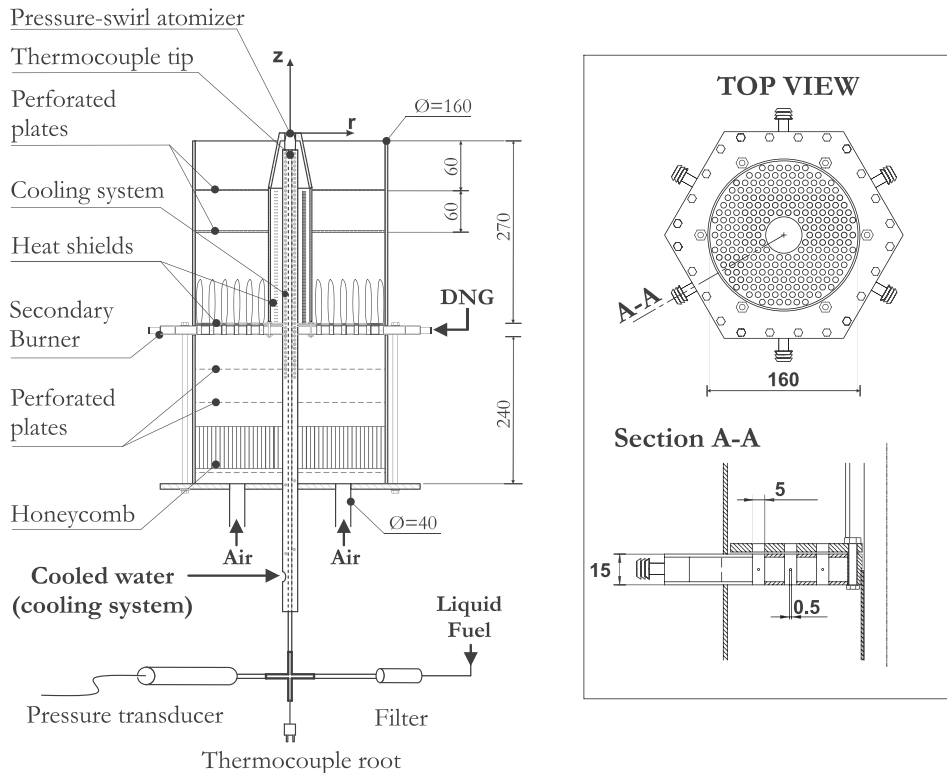


Fig. 1. Schematic of the burner facility with relevant dimensions in millimeters.

The ethanol spray is produced by a commercial pressure-swirl solid cone atomizer (Delavan WDA 0.5 GPH) with an 0.21 mm exit orifice and a 60° spray angle mounted on a 2 mm inner diameter stainless steel pipe through which liquid fuel is fed to the atomizer. During operation the burner components absorb a substantial amount of heat due to the high coflow temperature. In order to avoid pre-vaporization of the ethanol, a water-cooling system consisting of a helical copper coil was built around the stainless steel pipe through which ethanol fuel is fed. Ethanol temperature was monitored near the atomizer nozzle thread by a thermocouple Thermocoax Type K. The liquid injection pressure was measured online with a pressure transducer Omegadyne MMA. Acquisition of pressure data required dedicated electronics hardware to connect the pressure transducer output to the TSI EIC external data collection system board.

The air and DNG mass flow rates are set by Bronkhorst mass flow controllers with $\pm 0.5\%$ inaccuracy of full scale. The mass flow rate of the liquid fuel was set by a Coriolis flow meter with $\pm 0.5\%$ inaccuracy. The burner was mounted on a three-axis orthogonal traverse system controlled by stepper motors. Experimental equipment used remained in place and are described in Section 2.2. Throughout this paper, a r , z -coordinate system is used with its origin at the atomizer orifice exit plane. The convention of aligning 'z' with the axial direction and 'r' with the transverse direction is adopted.

2.2. Measurement techniques

In this study, five measurements techniques were separately employed: laser Doppler anemometry, phase Doppler anemometry, coherent anti-Stokes Raman spectroscopy and flue gas analyser. A brief description of each system used is given below.

2.2.1. Laser Doppler Anemometry (LDA)

LDA measurements were performed at $z = 0$ mm, i.e. at the atomizer orifice exit plane and, also, along the spray axis where

no droplets are present. The results provide the input boundary conditions needed for numerical simulations as well as relevant information to understand of the spray flame behavior. A two-dimensional LDA system was employed to measure simultaneously the axial and radial velocity components U_z and U_r , respectively. The LDA system consists of a 10 W Argon-ion laser, Bragg cell, probe head and a processor unit. A TSI 350 mm focal length lens collimated the laser beams emerging from the probe head yielding a probe volume of 0.17 mm in diameter and 2.40 mm in length. The scattered light from the seeding particles in the probe volume was collected in backscattering mode and guided to a FSA-3000 process unit. An additional TSI EIC external data collection system was used to record the analog output of the pressure transducer.

The air flow was seeded with alumina particles (Al_2O_3) by means of a cyclone system. The nominal particle median diameter is of 1 μm . At each measurement point 10^4 samples were acquired to ensure adequate convergence of the statistics. Velocity statistics were computed using the transit time as a weighting factor to compensate for the velocity bias (Albrecht et al., 2002). Consequently, the velocity statistics should be interpreted as Favre-averaged quantities (Oldenhof et al., 2011). According to the results of the detailed analysis of the various error sources in LDA measurements as reported by Absil (1995) we assumed that the mean velocity components are accurate up to 2% of the maximum flow velocity. The Reynolds normal stresses and the Reynolds shear stress are accurate up to 5% and 8% of their local maximum values, respectively.

2.2.2. Phase Doppler Anemometry (PDA)

A two-dimensional PDA system was employed to measure simultaneous droplet velocity and size statistics in the spray region. The laser, Bragg cell and probe head used were the same as in the LDA system described above. The receiver was set up in first-order refraction and had a 650 mm focal length receiving lens. The measurement volume was truncated by a 150 μm slit and the

signal fed into a FSA-4000 processor unit. The processor unit was also connected to a TSI EIC external data collection to collect the analog output of the pressure transducer.

Velocity and size statistics of a polydispersed ensemble of droplets can be significantly affected by adjustable parameters of the PDA measurement system (Albrecht et al., 2002). To ensure the reproducibility of the measurements, a parametric study of the adjustable operational parameters that influence the droplet diameter, droplet number density and velocity were performed prior to the experimental campaigns. The selected settings were kept constant throughout the measurements campaigns. The droplet density varies throughout the spray domain and the number of samples collected should be sufficient to achieve convergence of the statistical moments within a feasible measurement time. A total number of 10^4 samples were collected at positions with data rates lower than 10^2 Hz. For all the remain ensembles of 3×10^4 samples were acquired.

Based on the work of Widmann and Presser (2002), the inaccuracy associated with the droplet mean velocity is about 4%. Oscillations in the PDA response are found to occur for small droplets and results in different sizing error depending on the droplet diameter. According to the work of Taylor et al. (1994), sizing errors for droplets below $1 \mu\text{m}$ are on the order of 60%. Above $1 \mu\text{m}$, the sizing errors are approximately 8%. For further details on PDA errors and uncertainties we refer to the work of Friedmann and Renksizbulut (1999). The droplet diameter is estimated based on the phase shift between the Doppler signals and the droplet refractive index. For all cases studied, an estimation of the droplet temperature based on theoretical models of single-component droplet vaporization (Birouk and Gökarp, 2006) indicates that droplets are at boiling temperature at the first measurement station. Thus, the effect of temperature on the refractive index of ethanol is negligible and no systematic error in the droplet diameter is expected.

Smaller droplets follow faithfully the gas motion and were used to determine the gas-phase statistics. The selection of the droplet size representative of the gas motion was estimated by computing the first-and second-order statistics with different droplet size thresholds. For all cases in this study, droplets with diameter below $6 \mu\text{m}$ yielded minimal differences in the first and second order statistics and where chosen as representative of the gas motion. As will be shown later in Section 4.8, estimates of the Stokes number for different droplet size classes additionally confirm the selected droplet size threshold as suitable for tracers of the gaseous phase.

2.2.3. Coherent Anti-Stokes Raman Scattering (CARS)

The CARS system was employed to evaluate the gas-phase temperature statistics at $z = 0 \text{ mm}$ and in the spray region. A brief description of the CARS system and data post-processing procedure is reported here but for further details the reader is referred to van Veen and Roekaerts (2005, 2003). The ro-vibrational CARS system is based on an injection-seeded, frequency-doubled Nd:YAG laser (Spectron SL805 SLM), which yields 500 mJ per pulse at 532 nm with a pulse duration of 12 ns at 10 Hz repetition rate. In a planar-boxcars phase-matching configuration, a probe volume of $700 \mu\text{m}$ length and $35 \mu\text{m}$ diameter is obtained. The generated CARS radiation at the probe volume is focused onto the entrance of an echelle spectrometer, and the spectra dispersed on a CCD detector with 1100×330 pixels. The spectra are contained in two strips of 1100 intensity values, which are digitized by an 18-bit AD converter and stored. Dacapo software is used to normalize the CARS spectra using a nonresonant spectrum and fit to a library of theoretical, temperature-dependent spectra. Previous experiments show that single-shot imprecision of the system is 1–4% over a range from 2000 K to 300 K. The inaccuracy is estimated to be 20 K (van Veen and Roekaerts, 2005, 2003).

Three considerations were taken into account in the CARS measurements. First, the incidental presence of a droplet along the beams paths manifests itself as an increase of the N_2 CARS resonant signal background. A code was implemented in Dacapo software to evaluate and subtract a linear spectral background profile, interpolated between values found at the left- and right-hand sides of the spectrum before proceeding to the temperature evaluation. Secondly, a steep temperature gradient may occur over the probe volume, particularly near the reaction zone of the flame. In the presence of such a gradient, a substantially lower temperature than the mean temperature will be calculated due to the density effect. This was corrected based on a weighted fit according to the procedure suggested by van Veen and Roekaerts (2003). Last, at certain locations of the spray region, nonresonant signals were observed in addition to resonant N_2 signal. Based on the species present, only ethanol – having a large nonresonant susceptibility – can account for this signal. A quantitative analysis is not possible, but by the mere presence of nonresonant signals regions with fuel vapor can be identified qualitatively.

2.2.4. Flue gas analyser

Oxygen volume fraction measurements were performed at $z = 0 \text{ mm}$ with a Testo 335 fluegas analyser having a specified inaccuracy of $\pm 0.20\%$.

3. Cases description

The operating conditions as well as relevant dimensionless numbers of each individual flame studied are given in Table 1. The positions were the measurement techniques were employed are summarized in Table 2. Three spray flames in different coflow conditions were thoroughly studied. The three flames are denoted H_1 , H_2 and H_3 . In addition, some results are reported for two auxiliary cases H_1^{Aux} and H_2^{Aux} corresponding to sprays with higher liquid mass flow rates in identical hot-coflow conditions as H_1 and H_2 , respectively. These are included to elucidate the droplet velocity statistics in the near atomizer region and help the discussion of the flame lift-off behavior presented in Section 4.9. Only PDA measurements were made for these two cases. U_{cf} , T_{cf} and $\langle X_{\text{O}_2} \rangle$ represent the mass average velocity, temperature and oxygen volume fraction of the coflow, respectively. The values were determined by the measured velocity, temperature and oxygen volume fraction profiles at $z = 0 \text{ mm}$, i.e. at the atomizer orifice exit plane. The Weber number is defined as $\rho_g U_{jet}^2 l / \sigma$ and is identical for the three spray flames studied. l is the characteristic liquid film thickness and it was assumed to be equal to the nozzle diameter, i.e. $210 \mu\text{m}$. U_{jet} represents the difference between the estimated liquid jet velocity from the liquid mass flow rate and U_{cf} .

The coflow velocity profiles at $z = 0 \text{ mm}$ are displayed on Fig. 2. On the left-hand side, the coflow axial mean velocity $\langle U_z \rangle$ and the respective r.m.s. fluctuations u'_z are presented. The same quantities are shown for the radial velocity component on the right-hand side. It is observed that, on opposite sides of the spray, for all cases the magnitude of $\langle U_r \rangle$ sharply increases until a maxima in the near-wall of the central rod and then gradually decreases outwards. This indicates that the hot-diluted coflow has a strong inward velocity component and is being convected towards the spray axis filling in the void space between the ligaments and droplets formed at the center.

The r.m.s. fluctuations profiles of the axial and radial velocity components, u'_z and u'_r , show a sharp increase between $r = 70$ and 80 mm . This indicates that a shear layer is formed between the hot-diluted coflow and the laboratory air. Thus, the gradual mixing of laboratory air with the hot-diluted coflow causes changes in the radial profiles of temperature and oxygen concentration and,

Table 1

Burner operating conditions and dimensionless numbers of the flames studied. The pressure fluctuations are less than 0.2% for all flames.

Case	Coflow					Spray					ξ_{sr} [-]
	\dot{m}_{air} [kg/h]	\dot{m}_{DNG} [kg/h]	U_{cf} [m/s]	T_{cf} [K]	$\langle X_{O_2} \rangle$ [%]	\dot{m}_{Liq} [kg/h]	p [bar]	T_{Liq} [K]	U_{jet} [m/s]	We [-]	
H_I	70	3.28	3.42	1480	7.1	1.36	12.0	305	14.0	0.3	0.035
						1.53	15.9	304	15.7	0.4	0.037
H_{II}^{aux}	51	2.13	2.23	1300	9.3	1.46	11.5	301	14.9	0.4	0.048
						1.63	14.6	301	16.7	0.7	0.051
H_{III}	45	1.75	1.81	1225	10.1	1.48	11.7	298	15.1	0.5	0.052

Table 2

Summary of measurements locations for cases H_I , H_{II} and H_{III} .

Measurement technique	z (mm)	Comment
LDA	0, 20, 25, 30, 35, 40, 45, 50	Centerline, coflow radial profiles
CARS	0, 15, 20, 30, 40, 50, 60	Coflow radial profiles, spray region
Flue gas analyser	0	Coflow radial profiles
PDA	8, 10, 12, 15, 20, 30, 35, 40, 45	Spray region, steps of 1 mm

ultimately, perturbs the spray flame. It will be shown in Section 4.6 that up to $z = 60$ mm, the burner pipe diameter is wide enough to isolate the spray flame from the laboratory air entrainment.

Fig. 3 displays the coflow mean temperature $\langle T \rangle$ and r.m.s. fluctuations T' as well as the oxygen volume fraction $\langle X_{O_2} \rangle$ for the three cases presented in Table 1. For the cases studied, $\langle X_{O_2} \rangle$ radial profiles are fairly uniform over a significant radial distance in the coflow. In the temperature profiles, asymmetries are seen that exceed the inaccuracy of the CARS system. The maximum difference between the $\langle T \rangle_{max}$ at opposite sides of the spray is observed in case H_{II} and amounts to 34 K.

4. Results and discussion

4.1. Spray flames visual appearance and behavior

To show the overall flame appearance, color pictures are displayed in Fig. 4. The flames were photographed using a digital camera (Canon EOS X5) and have 0.6 s exposure time and identical aperture. The right inset shows a close-up of the spray region

and initial development of the flame. For all the flames presented, the field-of-view of the inset measures 170×160 mm 2 (width \times height).

It is observed that the atomizer yields conical spray flames. Based on the visual appearance, the spray flames in hot-diluted coflow are comprised of three regions: jet liquid break-up with no visible flame luminescence, a bluish reaction zone and a yellow zone farther downstream. The images shows that flame H_{III} has a stronger luminescence. Furthermore, a shorter flame length is observed as compared to flames H_I and H_{II} . For all the cases, the insets show a region of bright luminescence in the outer regions of the spray.

A study was performed to determine the lift-off height dependence on the liquid mass flow rates for the coflow conditions of case H_I , H_{II} and H_{III} . Experiments were also conducted for spray flames in air coflow and have been reported in Correia Rodrigues et al. (2014). In the current study, the procedure to determine the lift-off height was based on average flame luminescence from the photographs. It is defined as the axial distance from the atomizer orifice exit plane, $z = 0$ mm, to the lowest axial position of the bluish reaction zone along the spray axis.

The outcome is presented in Fig. 5 and the coflow conditions are presented in the inset. The test cases of this study are identified in the figure by the dashed squares. Case A_{II} , a reacting spray in air coflow, was previously described by the authors (Correia Rodrigues et al., 2014) and is also presented. When the liquid mass flow rates were below 1.10 kg/h, pre-vaporization of the ethanol occurred yielding a yellowish flame anchored at the atomizer orifice exit plane. Liquid mass flow rates higher than 1.70 kg/h could not be achieved with the current experimental setup.

As shown in Fig. 5, the lift-off height of sprays in hot-diluted conditions depends linearly on the liquid mass flow rate whereas in air coflow a non-linear dependence is observed. This is evidence

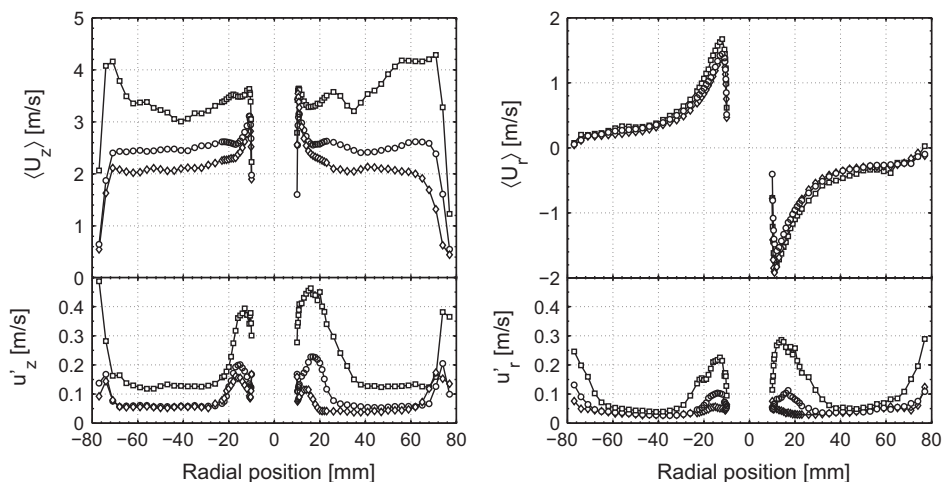


Fig. 2. Coflow mean velocities and r.m.s. fluctuations profiles of the axial and radial velocity components at $z = 0$ mm. (—□—: H_I , —○—: H_{II} , —◇—: H_{III}).

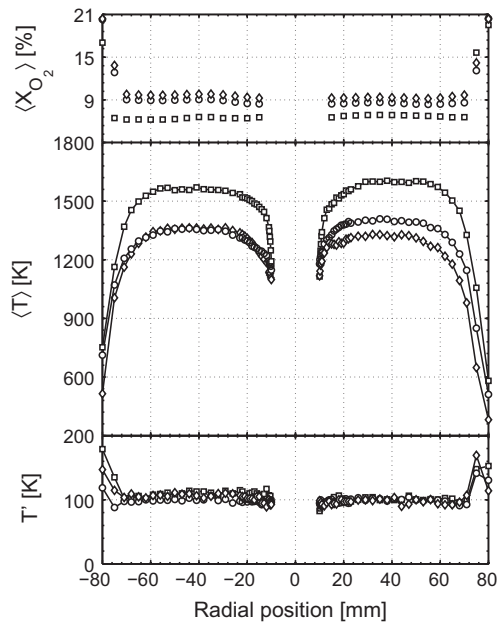


Fig. 3. Mean oxygen volume fraction $\langle X_{O_2} \rangle$, mean temperature $\langle T \rangle$ and root-mean-square temperature fluctuations T' profiles at $z = 0$ mm. (—□—: H_I , —○—: H_{II} , —◇—: H_{III}).

for the existence of different stabilization mechanics of the spray flames in hot-diluted coflow. Furthermore, it is observed that in the coflow conditions of case H_{III} , the lift-off height is more sensitive to the liquid mass flow rate than in the conditions of cases H_I and H_{II} .

Secondary breakup is not expected to play an important role in these flames. For the sprays in air coflow the Weber number varies from 2 to 3.4 and does not exceed a critical Weber number of 12 (based on Wierzba (1990)). Thus, in air coflow the secondary breakup is expected to be absent. In hot-diluted conditions, Weber numbers are smaller and within the range of liquid mass flow rates studied only vary from 0.2 to 0.5. Although, to our knowledge in the literature no information is available on the secondary breakup modes in the presence of strong evaporation rates, the ratio of the aerodynamic forces and surface tension remains significantly below unity and, therefore, no changes on the secondary breakup regime are expected.

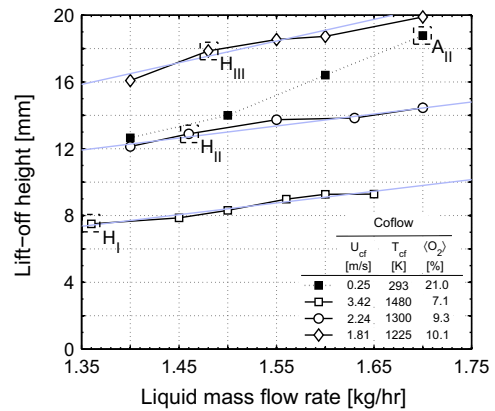


Fig. 5. Lift-off height dependence on the liquid fuel mass flow rate based on visual observations. The bulk properties of the coflow inlet are indicated in the table.

4.2. Droplet size and mean velocity field

Fig. 6 shows droplet Sauter mean diameter (d_{32}) and mean axial ($\langle U_z \rangle$) and radial ($\langle U_r \rangle$) velocity profiles for cases H_I , H_{II} and H_{III} at several axial stations. For flame H_I , no droplets are observed above the axial station of 30 mm. Regions in the spray core where no data are plotted correspond to positions where acquisition of sufficient amount of data within a reasonable measuring time was not possible.

The experimental results indicate that the initial d_{32} and velocity initial profiles as well as subsequent evolution downstream are similar for the three flames studied. At $z = 10$ mm the sprays are non-uniform with smaller d_{32} near the centerline and large d_{32} at the periphery. It is observed that droplets have a zero $\langle U_r \rangle$ close to the centerline. From the centerline until the spray periphery, $\langle U_r \rangle$ magnitude gradually increases until a maximum. This indicates that droplets are spreading into the hot-diluted coflow and it is in agreement with the visual appearance of the spray flames (see **Fig. 4** insets). With increasing radial distance, $\langle U_z \rangle$ increases until a maximum and then decreases to nearly the same magnitude as in the center region. For all the cases, a good symmetry of both velocity components and d_{32} is observed on opposite sides of the sprays axis.

With increasing axial distance from the atomizer, the center region of the sprays become void of droplets. As expected, this

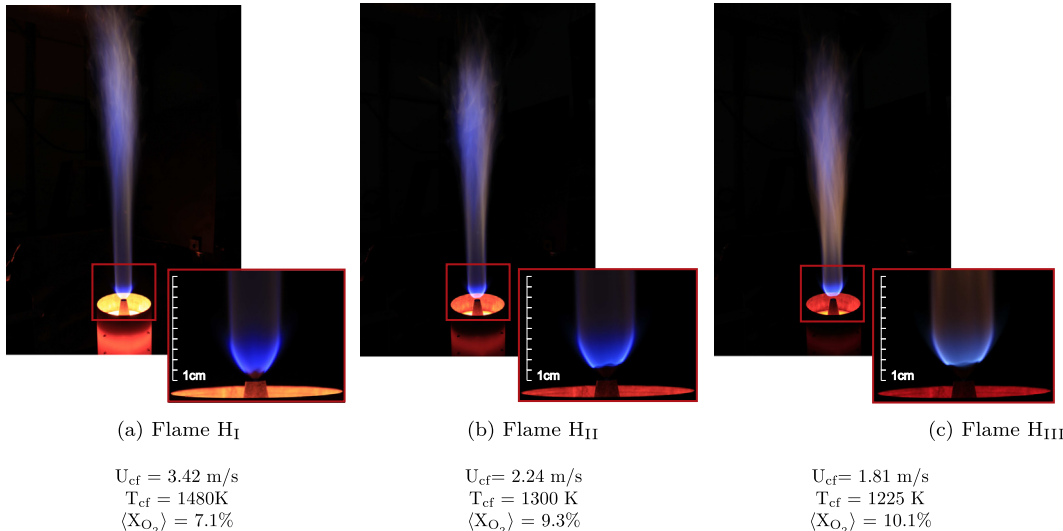


Fig. 4. Images of spray flames studied with 0.6 s exposure time and identical aperture. The bulk properties of the coflow inlet for each spray flame are listed below.

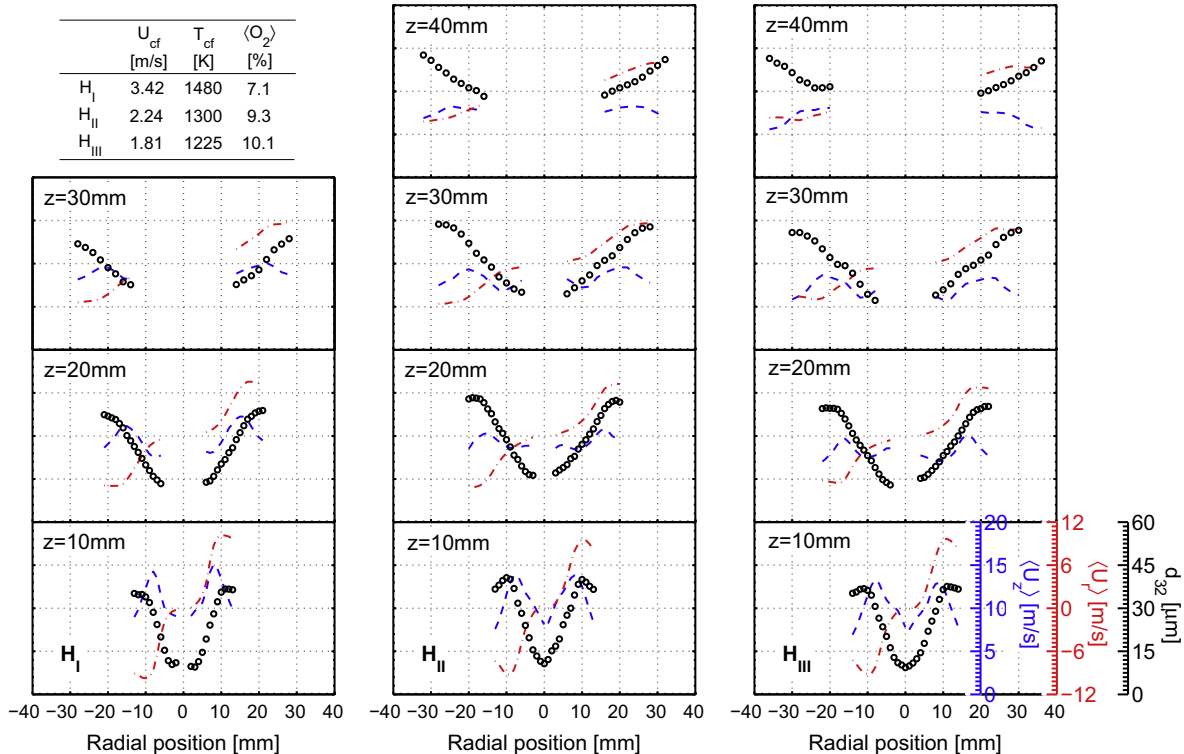


Fig. 6. Droplets Sauter mean diameter d_{32} and mean axial $\langle U_z \rangle$ and radial $\langle U_r \rangle$ velocity profiles at several axial stations. The different colored vertical axis scales display the aforementioned physical quantities. The upper and lower limits have been kept the same for the different axial stations. (—, $\langle U_z \rangle$, - - -, $\langle U_r \rangle$, ○, d_{32}).

effect is more pronounced for flame H_I since T_{cf} is the highest and droplets evaporate faster. A gradual reduction of the droplet velocity components is observed due to the momentum exchange of the droplets with the gaseous phase. An increase in the d_{32} between $z = 10$ mm and $z = 30$ mm is observed. The reason for is that small drag/inertial effects of large droplets leads to the displacement of the droplets outwards, progressively increasing the liquid fuel mass available in the spray peripherical regions of the spray.

4.3. Spray flames initial droplet distribution

To demonstrate the importance of the initial conditions on the overall spray morphology and development, the results of polydisperse ensemble of droplets at $z = 10$ mm is plotted in Fig. 7. The three radial positions selected correspond to the spray centerline, the radial position where the droplet number concentration is maximum (see Fig. 8) and the spray edge. For case H_I , no droplets are present at $r = 0$ mm and the radial position of 2 mm was selected as representative of the centerline. Droplet size frequency distribution curves (left y-axis) are overlaid with the corresponding cumulative droplet distribution curves (right y-axis). The distribution curves based on number of droplets per size class are represented by black lines whereas gray lines refer to volume size and can be related to mass by the liquid fuel density. Note that the droplet distribution based on volume are skewed to the right as expected due to the weighting effect of the larger droplets.

The results show clear differences between the droplet distributions at the radial positions presented, however, the trend among the three cases studied are in common. Flame H_I shows that, at $r = 2$ mm, 50% of the droplets are below 5 μm indicating that a high droplet surface area is available. 50% of the droplet mass is contained in the fraction below 18 μm . At larger radial distances from the spray centerline, $r = 6$ mm and $r = 13$ mm, the spread of the droplet number distribution increases and more larger droplets

are observed. The droplet diameter below which 50% of the mass is contained also increases.

Regarding flames H_{II} and H_{III} , it is observed that at all the three radial positions larger droplets are more abundant in the droplet size distributions than in H_I . At the centerline, $r = 0$ mm, 50% of the droplet mass resides in droplets below 28 μm and 24 μm for flame H_{II} and H_{III} , respectively. At $r = 6$ mm it can be noticed that, as compared to flame H_I , droplet number cumulative distributions do not change significantly. For the radial position of $r = 13$ mm and 14 mm a considerable number of large droplets is clearly observed and, therefore, more fuel mass is available at the spray periphery for cases H_{II} and H_{III} .

4.4. Droplet number density

The collection of liquid droplets spreads through the gaseous environment according to their initial momentum and droplet-gas interactions. Radial profiles of the droplet number density (n_d) at several axial stations are shown in Fig. 8 in order to elucidate the degree of dispersion and identify regions where gas-phase composition and momentum may be significantly influenced by the droplets presence.

For all cases, at $z = 10$ mm, n_d is nonuniform across the radial traverse and droplets mainly are concentrated at $r = 6$ mm. The subsequent development shows a broadening of the spray with increasing axial distance and a significant reduction of the droplet number density. Furthermore, in the region close to the spray axis no droplets are present. This effect is more significant for case H_I . In all the cases studied, the largest radial distance from the spray axis at which droplets are observed is nearly the same.

4.5. Gas-phase flow field

The evolution of the gas-phase mean axial $\langle U_z \rangle_g$ and radial $\langle U_r \rangle_g$ velocity components and normal $\langle u_z u_z \rangle_g$ and shear $\langle u_z u_r \rangle_g$ Reynolds

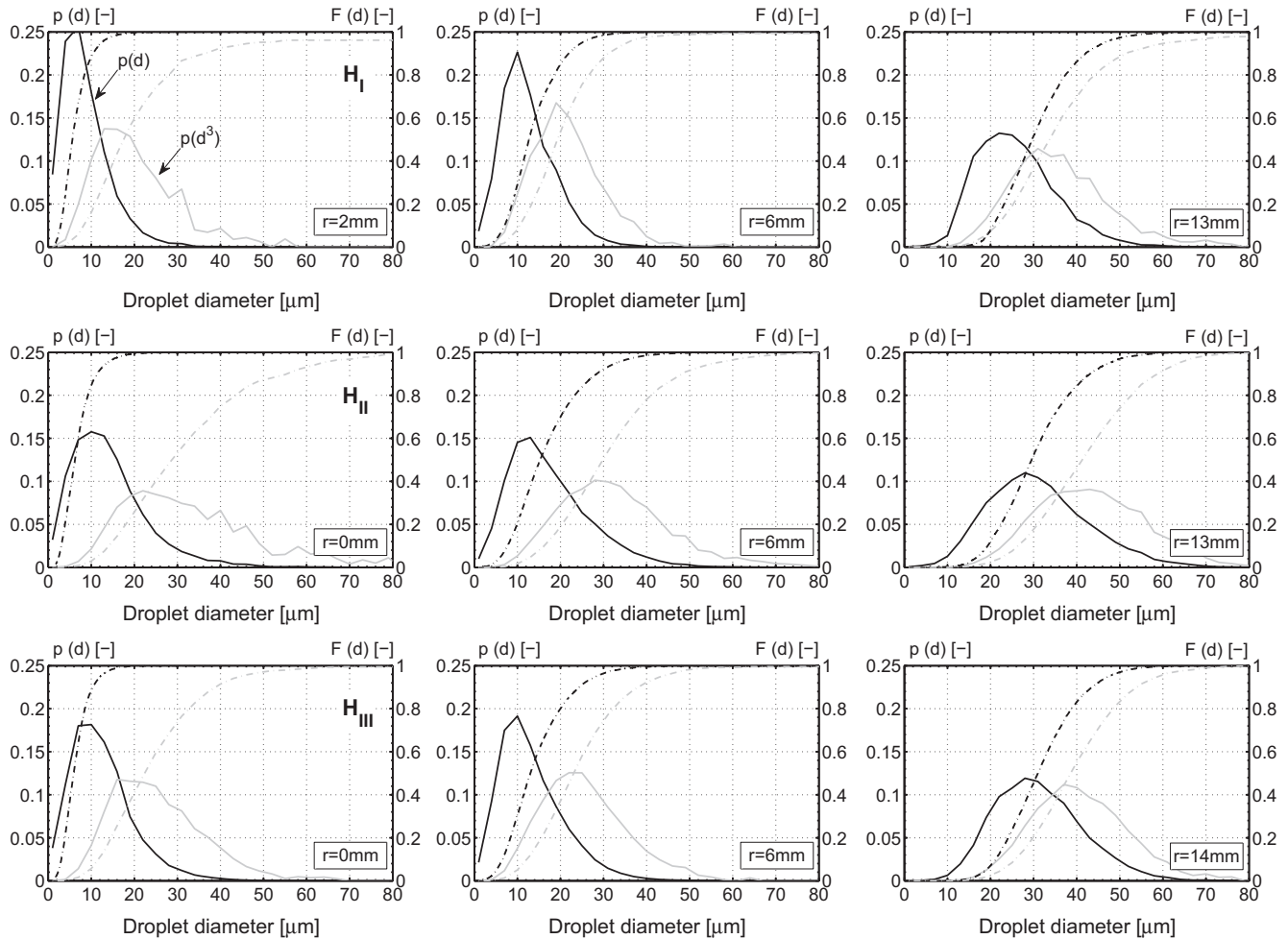


Fig. 7. Frequency distribution curves (solid lines) and cumulative droplet size distribution (dashed lines) based on number (d) and volume (d^3) at $z = 10$ mm for flames H_I , H_{II} and H_{III} .

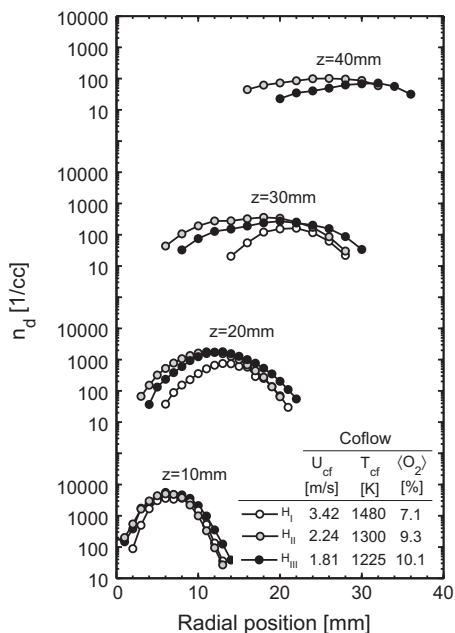


Fig. 8. Variation of droplet number density n_d with the radial distance measured at different axial positions for flames H_I , H_{II} and H_{III} .

stress profiles (Hanjalić and Launder, 2011) between four axial stations is displayed in Fig. 9. The subscript “g” denotes for the gas-phase. Each point presented in Fig. 9 is based on an ensemble of, at least, 100 samples. This threshold was found by investigating the convergence of the velocity mean and higher order statistical moments of droplets smaller than 6 μm as the number of samples increases. Notice that profiles of the physical quantities presented are similar for the different cases and the curves have been shifted for clarity. Due to the striking similarity among the profiles the following observations are common for all the three cases studied.

The $\langle U_z \rangle_g$ profiles indicate that at $z = 10$ mm a peak value occurs at about $r = 6$ mm. In the region around the centerline, $\langle U_z \rangle_g$ magnitude is close to the small droplets axial velocity (see Fig. 6) indicating that droplets move along with the gas flow field and no substantial momentum exchange through drag takes place in the center. At downstream axial stations, the $\langle U_z \rangle$ magnitude gradually decreases across the spray domain. This occurs as a result of the turbulent mixing with the entrained hot-diluted coflow. Moreover, the number droplet density is relatively high at this radial position. Hence, a modulation of the gas velocity field by the droplets is expected.

The $\langle U_r \rangle_g$ magnitude is one order of magnitude smaller than $\langle U_z \rangle_g$ at $z = 10$ mm. Further downstream, a reduction of the radial velocity component takes place to a nearly nil value. This shows that the gas flow field move mainly upwards and droplets shoot

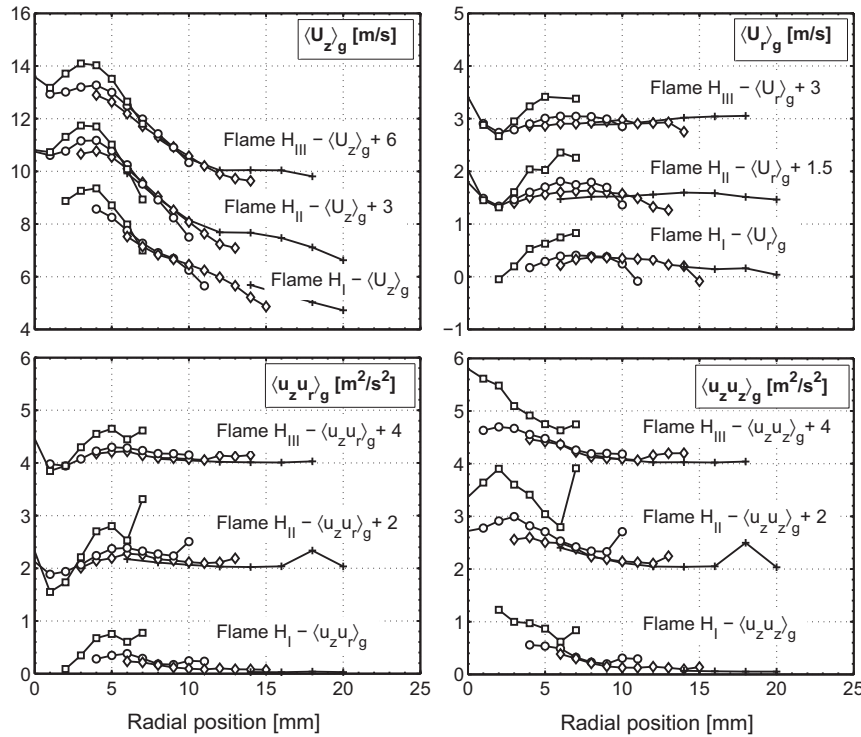


Fig. 9. Gas-phase mean axial $\langle U_z \rangle_g$ and radial velocity $\langle U_r \rangle_g$ along with Reynolds-stresses $\langle u_z u_r \rangle_g$ and $\langle u_z u_z \rangle_g$ at four axial stations for each flame studied. (—□—: $z = 10$ mm, —○—: $z = 15$ mm, —◇—: $z = 20$ mm, —+—: $z = 30$ mm).

outwards. Depending on their initial size diameter and momentum, the droplet trajectory path is deflected towards the direction parallel to the spray axis.

Both Reynolds-stresses, $\langle u_z u_z \rangle_g$ and $\langle u_z u_r \rangle_g$, are high close to the exit plane of the atomizer. Moreover, a large difference between $\langle u_z u_z \rangle_g$ and $\langle u_z u_r \rangle_g$ components is observed, with $\langle u_z u_z \rangle_g$ substantially higher than $\langle u_z u_r \rangle_g$. That can be attributed to the effect of liquid break-up in the dense region. Additionally, it indicates that significant mixing takes place in the near atomizer region. A fast decay of fluctuation levels until 30 mm is observed resulting in small anisotropy in the regions farther downstream.

Since the number of droplets is very low in the center region of the spray, LDA measurements were conducted along the spray centerline to determine the gas-phase velocity. The LDA system can measure the velocities of both 'seeding' particles that faithfully follow the gas-phase and of droplets. Therefore, 'cross-talk' from the velocity distribution of the droplets to that of the particles potentially results in velocity bias in the gas-phase statistics (Hardalupas and Taylor, 2004). The degree of bias will depend on the correlation between the particle and droplet arrival rate. In view of that, measurements were performed only in positions where no droplets are present, i.e. in the center region void of droplets. Additionally, prior to any further estimation of the flow velocity component, velocity distribution were meticulously studied to look for the evidence of outliers.

The evolution of gas-phase axial mean $\langle U_z \rangle_g$ and r.m.s. $u_z^g/\langle U_z \rangle_g$ fluctuations along the spray axis, is illustrated in Fig. 10 for the three flames studied. For all the flames, $\langle U_z \rangle_g$ gradually increases until $z = 60$ mm. As the flow is convected downstream, a mean gas acceleration in the center regions takes place due to turbulent diffusion of momentum from regions away from the center. The peak values of $\langle U_z \rangle_g$ for cases H_{II} and H_{III} exhibit a somewhat smaller magnitude than case H_I , reflecting the slower mixing rates in the center. The results of $u_z^g/\langle U_z \rangle_g$ indicate that turbulence levels in the centerline are substantially higher for flame H_I .

4.6. Gas-phase temperature field

The radial profiles of the gas-phase temperature statistics at four axial locations are shown in Fig. 11. On the left-hand side, the gas mean temperature $\langle T \rangle$ is presented along with the corresponding mean temperature gradient $(d\langle T \rangle/dr)$. On the right-hand side, the r.m.s. fluctuations T' are presented.

At $z = 15$ mm, the $\langle T \rangle$ profiles show a rise from the coflow to a single peak centered around $r = 14$ mm for all cases. From the peak temperature location towards the spray axis, $\langle T \rangle$ gradually

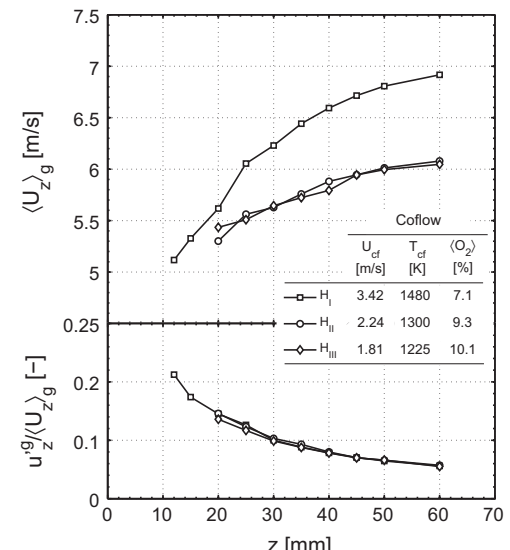


Fig. 10. Gas-phase mean axial velocity $\langle U_z \rangle_g$ and normalized r.m.s fluctuations $u_z^g/\langle U_z \rangle_g$ along the spray axis for flames H_I , H_{II} and H_{III} . (—□—: H_I , —○—: H_{II} , —◇—: H_{III}).

decreases to values lower than the ones observed in the coflow. However, in the region close to the spray centerline, $\langle T \rangle$ is significantly higher than the ethanol ignition temperature ($T_{ig} = 653$ K). The observed $\langle T \rangle$ profile shape can be attributed to the effects of evaporation and mixing prior to ignition as follows: due to the liquid atomization, an inward convective motion of the coflow is generated. The hot-diluted coflow is entrained into the spray and provides heat. The fuel vapor arises at the cost of heat losses from the oxidizing environment yielding lower gas-phase temperatures towards the spray axis. The mixture composition evolves from lean at the outer parts of the spray towards more rich at the center. Since the gas has relatively high temperature, the lean mixture at the spray outer parts ignites and the heat-release yields a peak in the $\langle T \rangle$. As one approaches the spray axis, the mean heat-release is lower and thus a decrease of $\langle T \rangle$ takes place. The peak $\langle T \rangle$ located at $r = 14$ mm is nearly identical for the three cases studied. This results from the combined effects of the coflow composition and temperature on the flame adiabatic temperature. The increase of the oxygen dilution in the oxidizer stream yields a reduction of the stoichiometric adiabatic temperature. However, a higher

oxygen dilution in the coflow is accompanied by an increase of the overall temperature of the oxidizer stream. Thus, the two effects cancel out and no substantial differences among the three cases are observed.

At $z = 20$ mm, three observations can be made. First, for all cases, the peak $\langle T \rangle$ shifts towards larger radial distance and it is located in a region of large droplets and low droplet number density (see Fig. 8, $17 < r < 20$ mm). This effect results in a decrease of the mean temperature gradient from the peak $\langle T \rangle$ towards the center as compared to $z = 10$ mm. Secondly, the mean temperatures in the region $0 < r < 15$ mm are highest for case H_I . This observation is in agreement with the sharper reduction of the droplet concentration in this region for case H_I (see Fig. 8). Lastly, throughout the flame region, the r.m.s. temperature fluctuation is rather similar among the three cases and the magnitude is overall higher by 75 K than in the hot-diluted coflow.

At higher axial stations, $z = 30$ and 40 mm, the displacement of the peak $\langle T \rangle$ towards larger radial distances proceeds due to the continuous spreading of the large droplets into the hot-diluted coflow. However, the distance between the peak and the spray axis

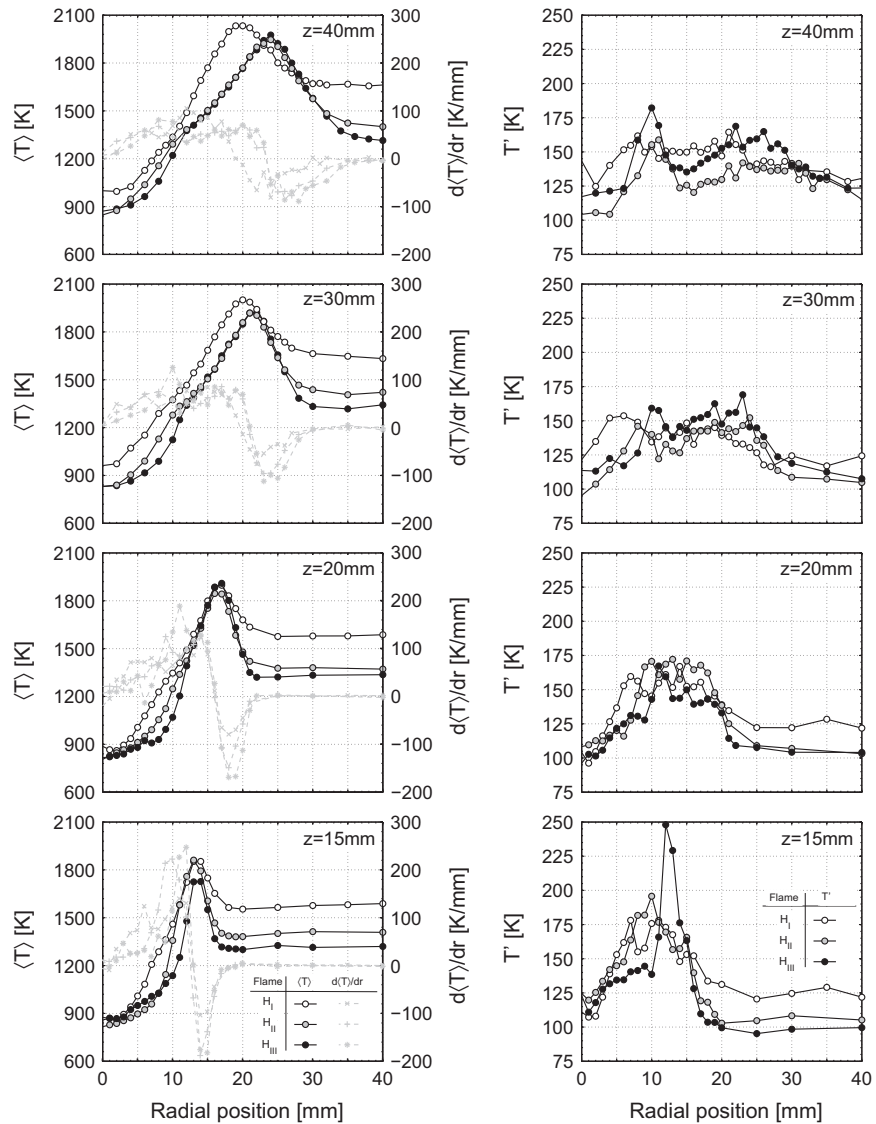


Fig. 11. Gas-phase mean temperatures $\langle T \rangle$ (left) and r.m.s. fluctuations T' (right) at four axial stations. The dashed gray lines correspond to the corresponding mean temperature gradients.

is smaller for case H_I . This indicates that spray flame H_I is narrower than the spray flames in H_{II} or H_{III} . This is in agreement with the photographs presented in Fig. 4.

At $z = 40$ mm, a peculiarity in the radial profiles of $\langle T \rangle$ and T' can be observed. This occurs more prominently in cases H_{II} and H_{III} and, therefore, a more detailed description is given. For these cases, between the radial positions $r = 0$ and $r = 10$ mm, T' increases to a local peak at $r = 10$ mm and then decreases to smaller values until $r = 15$ mm. Also, a significant change in the $\langle T \rangle$ slope takes place at $r = 10$ mm. An authors' early study describes the spray flame structure in air (case A_{II}) and in hot-diluted coflow (case H_{II}). In air coflow, an inner and an outer flame-front are present starting from the lift-off position and diverging with increasing downstream location (Correia Rodrigues et al., 2014). In the case of hot-diluted coflow (case H_{II}), the inner flame-front is weak. Due to the local mixture richness the heat-release is significantly smaller as compared to the outer flame-front and a local maxima in $\langle T \rangle$ is not observed. The results of Fig. 11 show that for different coflow temperature and oxygen dilution an inner flame-front exists in all cases. It would be worthwhile to investigate this in more detail using other laser diagnostics such as OH-Planar Laser Induced Fluorescence.

Fig. 11 shows additional information concerning the influence of air entrainment on the coflow inlet temperature profiles. It can be noticed that the coflow temperature at $r = 40$ mm remains nearly the same throughout the axial stations presented. This shows that, for the range of radial distances displayed, the burner pipe diameter is wide enough to isolate the spray flame from the laboratory air entrainment. CARS measurements at higher axial stations (not shown) indicate that above $z = 60$ mm the outer region of the spray flame is perturbed by the laboratory air. Thus, below $z = 60$ mm, the spray flame is stabilized only by the hot-diluted coflow. Above the axial station of 60 mm, the oxidizer stream consists of a mixture of laboratory air together with hot-diluted coflow and reaction zone weakening effects may be present (Medwell et al., 2009).

4.7. Gas-phase temperature histograms

The normalized temperature histograms of cases H_I , H_{II} and H_{III} at $z = 40$ mm are presented in Fig. 12. Five radial positions were selected for each case. The histogram corresponding to the radial position in the coflow core region is represented by a thicker line. The remaining positions correspond to the spray region. A bin size of 50 K was selected for all the histograms presented. The total number of samples in each histogram is 1000, except for $r = 0$ mm of case H_I where the number of valid samples was 120. For each of the five radial positions selected, the corresponding mean $\langle T \rangle$, root-mean-square temperature fluctuation T' as well as skewness (S) and kurtosis (K) of the temperature distribution are listed in the table inset.

At the radial positions where the peak $\langle T \rangle$ is observed ($r = 20$, 24 and 24 mm for cases H_I , H_{II} and H_{III} , respectively), the temperature distribution are nearly symmetric ($S = 0$) and broad with temperatures ranging from 2400 K down to 1400 K. A considerable amount of samples are over 2000 K for all cases. It is observed that the number of valid samples above 2000 K is greater for case H_I . This is related to the higher temperature of the oxidizer coflow.

For all cases, the radial position of 15 mm is located between the inner and outer flame-front. As expected, lower temperature samples are present in the temperature distributions. As compared to the radial positions where the peak $\langle T \rangle$ occurs, a substantial reduction of the number of valid samples above 2000 K is observed. For case H_I , a substantial amount of valid samples above 2000 K still persist at this position, yet, it is significantly reduced as compared to $r = 20$ mm. These results suggest that the coflow

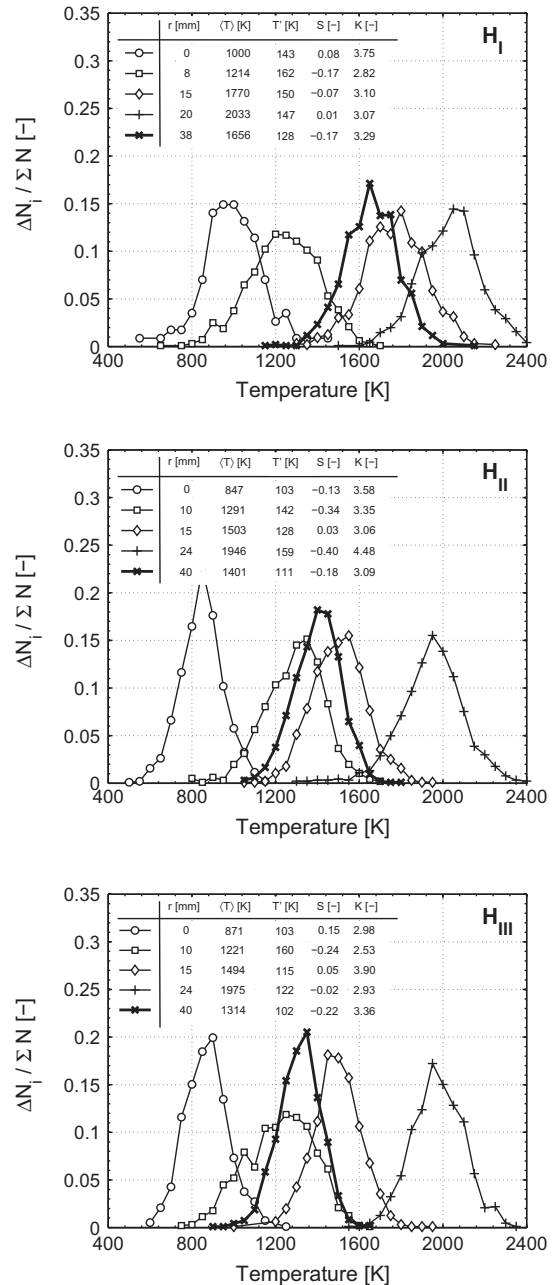


Fig. 12. Normalized temperature histograms for five radial positions at $z = 40$ mm for cases H_I , H_{II} and H_{III} .

temperature is the driving parameter with respect to the outer flame-front temperature peaks.

At the spray axis, $r = 0$ mm, the temperature distributions are symmetric and samples are below 1200 K for all cases. Temperature histograms at $z = 20$ mm and 30 mm (not shown) have virtually identical r.m.s. and skewness value. This indicates that in the region close to the spray axis only turbulent mixing occurs and the gas-phase is rather homogeneous.

4.8. Droplet-size class properties

Figs. 13 and 14 show the mean axial $\langle U_z \rangle$ and radial $\langle U_r \rangle$ velocity components of four droplet size-classes at three axial stations, $z = 10$, 20 and 30 mm. The class width was chosen as 10 μm . All the points are an average of at least 200 samples. The droplets in the size class between 0 and 6 μm are considered to be flow

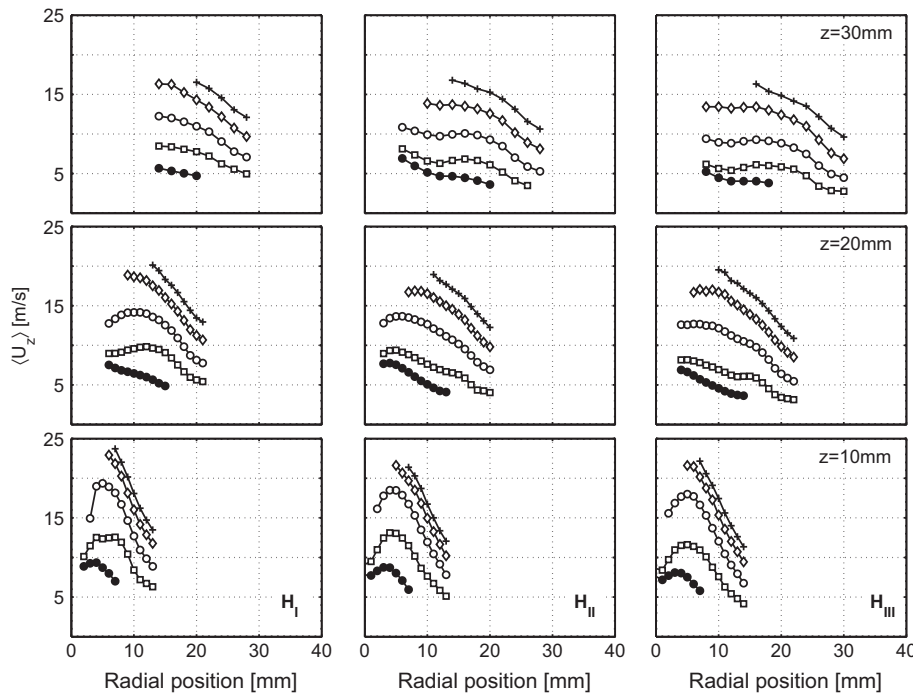


Fig. 13. Radial profiles of the conditioned droplet mean axial velocity ($\langle U_z \rangle$) for three axial stations. (—●—: Gas-phase ($d \leq 6\text{ }\mu\text{m}$), —□—: $10\text{ }\mu\text{m} \leq d < 20\text{ }\mu\text{m}$, —○—: $20\text{ }\mu\text{m} \leq d < 30\text{ }\mu\text{m}$, —◇—: $30\text{ }\mu\text{m} \leq d < 40\text{ }\mu\text{m}$, —+—: $40\text{ }\mu\text{m} \leq d < 50\text{ }\mu\text{m}$).

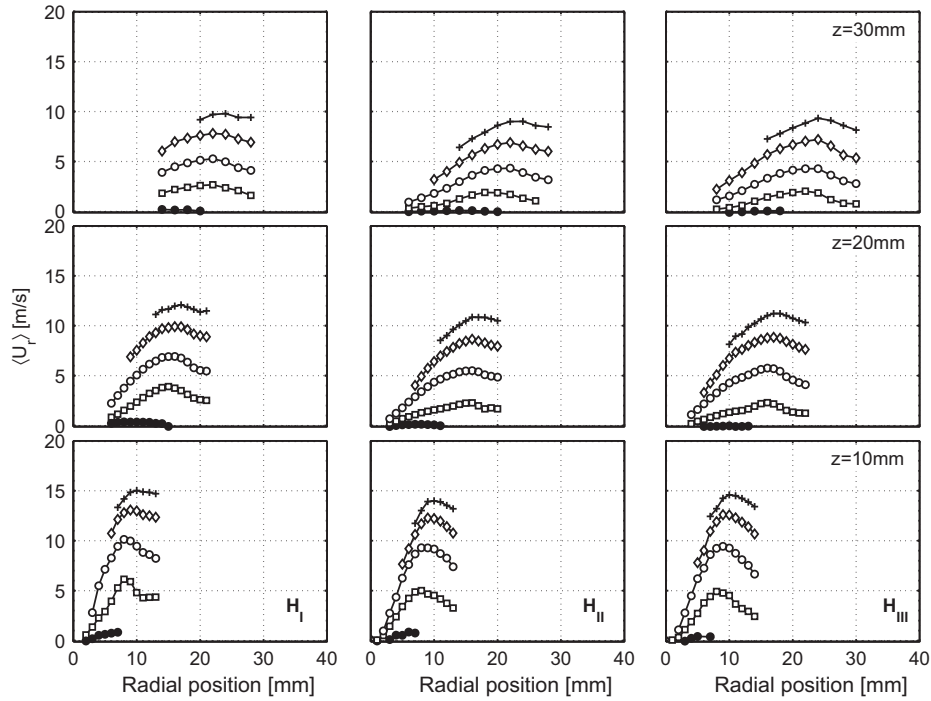


Fig. 14. Radial profiles of the conditioned droplet mean axial velocity ($\langle U_z \rangle$) for three axial stations. (—●—: Gas-phase ($d \leq 6\text{ }\mu\text{m}$), —□—: $10\text{ }\mu\text{m} \leq d < 20\text{ }\mu\text{m}$, —○—: $20\text{ }\mu\text{m} \leq d < 30\text{ }\mu\text{m}$, —◇—: $30\text{ }\mu\text{m} \leq d < 40\text{ }\mu\text{m}$, —+—: $40\text{ }\mu\text{m} \leq d < 50\text{ }\mu\text{m}$).

tracers. The mean velocity of this size class thus represents the gas-phase mean velocity. The difference between the mean velocity for a particular size class and the gas-phase mean velocity will be referred to as slip velocity.

The development of droplet $\langle U_z \rangle$ along the several axial stations shows similar trends for cases H_I , H_{II} and H_{III} . At $z = 10\text{ mm}$, an increase of droplet slip velocity with the size-class is observed. Farther downstream, slip velocity gradually decreases for the different droplet size-classes. Identical observations can be made regarding

the droplet $\langle U_r \rangle$ component. This occurs because the momentum of the liquid droplets is transferred to the gaseous phase through drag and evaporation.

4.9. Discussion of the flame structure and lift-off behavior

This section presents a discussion on the droplet dispersion, flame structure and lift-off behavior of spray flame in hot-diluted coflow conditions. Before proceeding with the analysis, it is of

Table 3

Relevant dimensionless numbers and relaxation time scales for different droplet size classes.

	Size-class (μm)	Cases				
		H_I	H_{II}	H_{III}	H_I^{Aux}	H_{II}^{Aux}
$We_d [-]$	10–20	0.0	0.0	0.0	0.0	0.0
	20–30	0.1	0.1	0.1	0.1	0.1
	30–40	0.1	0.2	0.2	0.2	0.2
	40–50	0.2	0.2	0.2	0.3	0.3
$Re_d [-]$	10–20	0	1	1	1	1
	20–30	1	2	2	2	2
	30–40	2	3	4	3	4
	40–50	3	4	5	4	5
$St_d [-]$	0–6	0.5	0.5	0.5	0.5	0.5
	10–20	11	13	13	14	14
	20–30	32	36	38	36	40
	30–40	62	70	75	70	78
	40–50	102	116	124	115	129
$\tau_d [\text{ms}]$	0–6	0.01	0.01	0.01	0.01	0.01
	10–20	0.17	0.18	0.19	0.17	0.18
	20–30	0.47	0.50	0.53	0.47	0.50
	30–40	0.93	0.99	1.63	0.93	0.99
	40–50	1.54	1.63	1.72	1.54	1.63

interest to discuss in detail relevant dimensionless numbers characterizing the droplet motion.

4.9.1. Relevant dimensionless numbers

Some relevant dimensionless numbers are listed in [Table 3](#) for each of the size classes and for the droplets smaller than 6 μm that are representative of the statistics of the gas-phase. The droplet Weber number (We_d) was determined as $\rho_g U_j^2 d_c / \sigma$. Here, ρ_g represents the gaseous phase density, d_c is the mean droplet diameter of the selected size class and U_j the difference between the maximum droplet (U_z) measured at $z = 10$ mm and the bulk coflow velocity. The gas properties were determined from the coflow bulk temperature and composition. As can be observed in [Table 3](#), We_d is well below unity for all droplet size classes suggesting that small droplets resulting from the secondary breakup are absent for all five cases.

The droplet Reynolds number (Re_d) was determined as $U_j d_c / v_g$. Assuming that droplets are spherical and move in a viscous flow at a very low Reynolds number, the relaxation time (τ_d) can be determined as $\rho_d d_d^2 / 18\mu_g$. Here, ρ_d and μ_g are the droplet density and the gaseous phase dynamic viscosity, respectively. As shown in [Table 3](#), for droplets below 10 μm the Re_d is well below one whereas for droplets bigger than 30 μm the highest value encountered for Re_d is of 5. Hence, larger droplets incur an underestimation of the droplet relaxation time by at most 7%. On the other hand, droplets with a diameter smaller than 10 μm satisfy the assumption of Stokes flow.

The Stokes number (St_d) is defined as the ratio of the characteristic time of a droplet to a characteristic time of the flow and indicates the different regimes of droplet dispersion for each droplet size class ([Eaton and Fessler, 1994](#); [Wood et al., 2005](#)). The flow characteristic time was defined as d_{at}/U_{at} where d_{at} is the atomizer nozzle diameter and U_{at} the estimated liquid jet velocity in the atomizer nozzle. [Table 3](#) shows that for all cases studied, droplets bigger than 10 μm have $St_d \gg 1$ and therefore do not follow changes in the flow field. For droplets with diameter smaller than 6 μm , the droplet response time is faster than the flow characteristic time scale and, therefore, behave as flow tracers.

4.9.2. Flame structure

[Fig. 15](#) presents a schematic of the spray structure in hot-diluted coflow conditions and, together with [Table 3](#), can be used to describe the droplet dispersion and the flame structure. As a

result of the spray breakup, droplets spread outwards and an outer flame-front develops wherein low droplet concentration and large droplets prevail. The outward ballistic motion of the droplets results from the droplet initial radial velocity as well as the correspondent large St values and is the mechanism responsible for the flame inverted conical shape. As shown in [Table 3](#), droplets bigger than 10 μm have Stokes number sufficiently large to not follow changes in the flow field. Thus, as the spray evolves downstream, large droplets move outwards and a flammable mixture resulting from the entrained hot oxidizing coflow and the fuel vapor is formed at increasing larger radial distances. A comparison of cases H_I and H_{III} additionally shows highest Stokes number for droplets within the same size class when the coflow temperature is lowest (H_{III}). Hence, lower coflow temperatures yields a deeper penetration of droplets into the hot-diluted coflow and, consequently, the flames become wider. This is in agreement with the visual observations, namely the flame of case H_{III} is slightly wider than that of H_I (see [Fig. 4](#) insets).

4.9.3. Characteristic scales and lift-off behavior

The trends presented in [Fig. 5](#) show that the lift-off height decreases for increasing bulk coflow temperatures while it increases with increasing liquid mass flow rates. This section presents a possible explanation of the lift-off behavior of spray flames in hot-diluted coflow. As proposed by [Delabroy et al. \(1998\)](#) and [Martínez-Ruiz et al. \(2013\)](#), in a reacting spray, the time needed for combustion to take place is determined by the time scales of three phenomena: (1) droplet vaporization, (2) droplet convection, and (3) the chemical reaction. The comparison of the different time scales allows to characterize the lift-off height behavior of the spray flame. Estimates of characteristic numbers for different droplets size classes are presented in [Table 4](#). The following discussion is based on single droplet theory and the interdroplet interaction effects are neglected ([Zoby et al., 2011](#); [Miyasaka and Law, 1981](#)). For all the calculations, the gas properties were determined from the coflow bulk temperature and composition.

The droplet vaporization time scale (t_{vap}) was estimated by the d^2 law ([Law, 1982](#); [Birouk and Gökalp, 2006](#)). It is considered that droplets emerge from the atomizer nozzle at the boiling point and, therefore, a droplet heat-up period is absent. For an evaporating spherical droplet in a flow, t_{vap} can be written as d_0^2/K . K is the vaporization constant and is given by $-4/\rho_l [\rho_m D_m Sh_m \ln(1 + B_M)]$. This model accounts for the slip velocity between the gas and

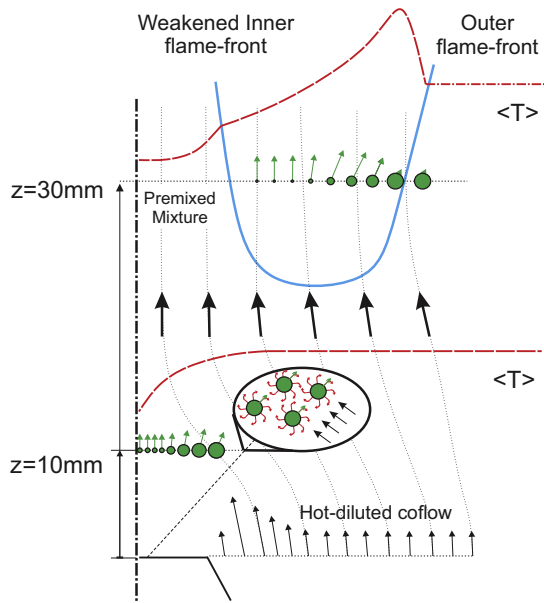


Fig. 15. Schematic of the gas and droplet motion of pressure-swirl sprays in hot-diluted coflow conditions.

droplet motion. The gas-phase properties values 'm' were evaluated by the 1/3-rule (Chen and Pereira, 1996). D is the binary diffusion coefficient of ethanol and air at condition (T_m , Y_m). Sh is the Sherwood number and B_M represents the Spalding mass transfer number. Immediately after the atomizer nozzle exit plane, the droplets travel a certain path and leave behind a wake of fuel vapor that depends on the vaporization rates. Since the chemical reaction cannot begin until the gaseous fuel is generated and mixed, the vaporization time (t_{vap}) together with droplet convective time scale (t_{conv}) are two important scales influencing the lift-off location. An estimation of t_{conv} was computed as $z_{10\text{ mm}}/U_{z10}$. Here, U_{z10} represents the velocity different between measured droplet (U_z) at the spray periphery at $z = 10\text{ mm}$ and U_{cf} . A characteristic chemical time scale (t_{ch}) for the ethanol flame in hot coflow conditions was evaluated using calculations of transient counterflow diffusion flames. The strain rate was set to a representative value of 100 s^{-1} . The calculation started from the profile of a steady non-reaction flamelet (mixing only) and the chemical time t_{ch} was defined as

the time needed to reach the moment of maximal rate of temperature increase. The Chem1D code was used (CHEM1D) using the Marinov chemical mechanism (Marinov, 1999). For the three cases, fuel vapor at the boiling temperature was used as fuel and the hot-diluted coflow as oxidizer. The evolution of the temperature as function of time at the stoichiometric mixture fraction was used to estimate a characteristic chemical time scale for each of the three cases.

A comparison between cases H_I , H_{II} and H_{III} shows no substantial differences on the droplets convective time scale. However, significant differences are observed in the droplets vaporization and in the chemical time scales. For droplets smaller than $30\text{ }\mu\text{m}$, t_{vap} is lower than t_{conv} by almost one order of magnitude. This indicates that substantial vaporization of droplets smaller than $30\text{ }\mu\text{m}$ occurs prior to the lift-off location. As expected, larger droplets survive the near-injector region due to their larger Stokes number and spread into the hot-diluted coflow.

For the highest coflow temperature (case H_I), droplets smaller than $10\text{ }\mu\text{m}$ have t_{vap} of the same order of magnitude as that of t_{ch} . Furthermore, t_{vap} and t_{ch} are considerably smaller than t_{conv} . This indicates that chemical reaction engages almost immediately after the gaseous fuel is generated from the small droplets in the near-injector region and the vapor fuel availability is the limiting factor to form an ignitable mixture. The lower coflow bulk temperatures of cases H_{II} and H_{III} yield an increase of the t_{vap} and, consequently, less fuel vapor is available prior to the lift-off location. A comparison between the different droplet size classes of case H_I and H_{III} show a reduction of about 60% in the vaporization time scales for droplets in the size class of $20\text{--}30\text{ }\mu\text{m}$ and of 30% for droplets in the size class of $40\text{--}50\text{ }\mu\text{m}$ (see bold values in Table 4). The chemical time scale increases by more than one order of magnitude and is noticeably bigger than t_{vap} or t_{conv} . It thus can be understood that for case H_{II} and H_{III} , both t_{vap} and t_{ch} contribute to an increase of the lift-off height, however, t_{ch} has a more prominent effect.

The impact of the liquid mass flows on the lift-off height can be assessed by comparing case H_I with H_I^{Aux} and H_{II} with H_{II}^{Aux} . Increase of the liquid mass flows (and, therefore, higher liquid jet momentum) yields a decrease of t_{conv} due to the higher droplet initial velocity. However, only a slight change is observed in the vaporization rates. Hence, the concentration of fuel vapor in the droplets wake until $z = 10\text{ mm}$ is smaller and, consequently, a larger droplet path is required to form a flammable mixture. This manifests itself as an increase of the lift-off height.

5. Conclusions

A comprehensive study was carried out of ethanol sprays issuing into hot-diluted coflows with different conditions. LDA, PDA and CARS techniques were employed to study spray flame structure and provide an explanation of the stabilization characteristics of sprays combustion under Mild conditions. An extensive database was obtained for validation of numerical simulations.

For pressure-swirl sprays with identical Weber number the results indicate that within the coflow conditions studied the initial droplet velocity and d_{32} distribution do not differ significantly. Small droplets are present at the center and quickly evaporate as the spray evolves downstream. Large droplets with relatively high Stokes number move outwards and penetrate into the hot-diluted coflow. The fuel vapor originated from the large droplets mixes with the hot-diluted coflow and a lean flame-front develops in a region of low droplet concentration at the spray outer parts. The temperature histograms in this region show a considerable amount of samples over 2000 K . Lower coflow bulk temperature yields a reduction of the peak temperatures in the lean flame-front at the

Table 4
Estimates of the characteristics time scales for different droplet size classes.

	Size-class (μm)	Cases				
		H_I	H_{II}	H_{III}	H_I^{Aux}	H_{II}^{Aux}
t_{vap} [ms]	10–20	0.21	0.31	0.35	0.21	0.30
	20–30	0.64	0.81	0.77	0.63	0.77
	30–40	1.21	1.48	1.62	1.17	1.41
	40–50	1.91	2.29	2.50	1.85	2.18
t_{conv} [ms]	10–20	3.47	3.50	4.26	2.65	2.61
	20–30	1.84	1.80	2.02	1.36	1.18
	30–40	1.20	1.25	1.31	0.96	0.90
	40–50	0.99	1.02	1.05	0.82	0.76
t_{ch} [ms]	all	0.31	2.32	4.93	0.31	2.32
t_{vap}/t_{conv} [-]	10–20	0.06	0.09	0.08	0.08	0.11
	20–30	0.35	0.45	0.45	0.46	0.65
	30–40	1.01	1.18	1.24	1.22	1.57
	40–50	1.92	2.25	2.39	2.24	2.88
t_{ch}/t_{vap} [-]	10–20	1.48	7.48	14.09	1.48	7.73
	20–30	0.48	2.86	5.48	0.49	3.01
	30–40	0.26	1.57	3.04	0.26	1.65
	40–50	0.16	1.01	1.97	0.17	1.06

spray outer parts suggesting that the oxidizer stream temperature is the driving parameter with respect to the peak temperatures. Due to the initial droplet concentration distribution, the gas composition becomes increasingly rich towards the spray axis. A secondary flame-front significantly weakened due to the local richness of the gas composition is also observed close to the spray center region for all the cases studied. It is shown that the observed increase of the lift-off height for lower coflow bulk temperatures is related to the increase of the droplet vaporization time scale and an increase of the chemical time scale.

References

Absil, L.H.J., 1995. Analysis of the Laser Doppler Measurement Technique for Application in Turbulent Flows. PhD Thesis, Delft University of Technology.

Albrecht, H.E., Damaschke, N., Borys, M., Tropea, C., 2002. *Laser Doppler and Phase Doppler Measurement Techniques*, first ed. Springer.

Barlow, R.S., 2007. Laser diagnostics and their interplay with computations to understand turbulent combustion. *Proc. Combust. Inst.* 31, 49–75.

Birouk, M., Gökalp, I., 2006. Current status of droplet evaporation in turbulent flows. *Prog. Energy Combust.* 32 (4), 408–423.

Cavalieri, A., de Joannon, M., 2004. Mild combustion. *Prog. Energy Combust. Sci.* 30, 329–366.

Cessou, A., Stepowski, D., 1996. Planar laser induced fluorescence measurement of OH in the stabilization stage of a spray jet flame. *Combust. Sci. Technol.* 118, 361–381.

CHEM1D. A One-dimensional Laminar Flame Code. Eindhoven University of Technology. <<http://www.combustion.tue.nl/chem1d/>>.

Chen, X.-Q., Pereira, J.C.F., 1996. Computation of turbulent evaporating sprays with well-specified measurements: a sensitivity study on droplet properties. *Int. J. Heat Mass Transfer* 39 (3), 441–454.

Coelho, P.J., Peters, N., 2001. Numerical simulation of a mild combustion burner. *Combust. Flame* 124, 503–518.

Correia Rodrigues, H., Tummers, M.J., van Veen, E.H., Roekaerts, D.J.E.M., 2014. Spray flame structure in conventional and hot-diluted combustion regime. *Combust. Flame*, 2014, <http://dx.doi.org/10.1016/j.combustflame.2014.07.033>.

Dally, B.B., Karpetis, A.N., Barlow, R.S., 2002. Structure of turbulent nonpremixed jet flames in a diluted hot coflow. *Proc. Combust. Inst.* 29, 1147–1154.

Delabroy, O., Lacas, F., Labegorre, B., Samaniego, J.-M., 1998. Paramètres de similitude pour la combustion diphasique. *Rev. Gén. Therm.* 37, 934–953.

Derudi, M., Rota, R., 2011. Experimental study of the mild combustion of liquid hydrocarbons. *Proc. Combust. Inst.* 33 (2), 3325–3332.

Eaton, J.K., Fessler, J.R., 1994. Preferential concentration of particles by turbulence. *Int. J. Multiphase Flow* 20 (Supplement 1(0)), 169–209.

Friedmann, J.A., Renksizbulut, M., 1999. *Combust. Flame* 117, 661–684.

Goix, P.J., Edwards, C.F., Cessou, A., Dunsby, C.M., Stepowski, D., 1994. Structure of a methanol/air coaxial reacting spray near the stabilization region. *Combust. Flame* 98, 205–219.

Hanjalić, K., Launder, B., 2011. *Modelling Turbulence in Engineering and the Environment*, first ed. Cambridge University Press.

Hardalupas, Y., Taylor, A.M.K.P., 2004. The identification of LDA seeding particles by the phase-doppler technique. *Exp. Fluids* 6 (2), 137–140.

Ihme, M., See, Y.C., 2011. LES flamelet modeling of a three-stream MILD combustor: analysis of flame sensitivity to scalar inflow conditions. *Proc. Combust. Inst.* 33 (1), 1309–1317.

Jenny, P., Roekaerts, D.J.E.M., Beishuizen, N., 2012. Modeling of turbulent dilute spray combustion. *Prog. Energy Combust. Sci.* 38 (6), 846–887.

Law, C.K., 1982. Recent advances in droplet vaporization and combustion. *Prog. Energy Combust. Sci.* 8 (3), 171–201.

Marinov, N.M., 1999. *Int. J. Chem. Kinet.* 31 (3), 183–220.

Martínez-Ruiz, D., Urvay, J., Sánchez, A.L., Liñán, A., Williams, F.A., 2013. Dynamics of thermal ignition of spray flames in mixing layers. *J. Fluid Mech.* 734, 387–423.

Medwell, P.R., Dally, B.B., 2012. Effect of fuel composition on jet flames in a heated and diluted oxidant stream. *Combust. Flame* 159 (10), 3138–3145.

Medwell, P.R., Paul, R., Kalt, P.A.M., Dally, B.B., 2007. Simultaneous imaging of OH, formaldehyde, and temperature of turbulent nonpremixed jet flames in a heated and diluted coflow. *Combust. Flame* 148 (12), 48–61.

Medwell, P.R., Paul, R., Kalt, P.A.M., Dally, B.B., 2009. Reaction zone weakening effects under hot and diluted oxidant stream conditions. *Combust. Sci. Technol.* 181 (7), 937–953.

Miyasaka, K., Law, C.K., 1981. Combustion of strongly-interacting linear droplet arrays. *Proc. Combust. Inst.* 18 (1), 283–292.

Oldenhof, E., Tummers, M.J., van Veen, E.H., Roekaerts, D.J.E.M., 2010. Ignition kernel formation and lift-off behaviour of jet-in-hot-coflow flames. *Combust. Flame* 157, 1037–1234.

Oldenhof, E., Tummers, M.J., van Veen, E.H., Roekaerts, D.J.E.M., 2011. Role of entrainment in the stabilisation of jet-in-hot-coflow flames. *Combust. Flame* 158 (8), 1553–1563.

Oldenhof, E., Tummers, M.J., van Veen, E.H., Roekaerts, D.J.E.M., 2013. Conditional flow field statistics of jet-in-hot-coflow flames. *Combust. Flame* 160 (8), 1428–1440.

O'Loughlin, W., Masri, A.R., 2011. A new burner for studying auto-ignition in turbulent dilute sprays. *Combust. Flame* 158 (8), 1577–1590.

Röhl, O., Peters, N., 2009. A reduced mechanism for ethanol oxidation. In: *Proceedings of 4th European Combustion Meeting*, Vienna University of Technology, Vienna, Austria, 2009.

Stepowski, D., Cessou, A., Goix, P., 1994. Flame stabilization and OH fluorescence mapping of the combustion structures in the near field of a spray jet. *Combust. Flame* 99 (3–4), 516.

Taylor, P., Dudek, R., Flaherty, D., Kaempfe, T., 1994. *J. Aerosol Sci.* 25 (2), 419–423.

Tsuji, H., Gupta, A.K., Hasegawa, T., Katsuki, M., Kishimoto, K., Morita, M., 2002. *High Temperature Air Combustion: From Energy Conservation to Pollution Reduction*, first ed. CRC.

van Veen, E.H., Roekaerts, D.J.E.M., 2003. On the accuracy of temperature measurements in turbulent jet diffusion flames by coherent anti-stokes-raman spectroscopy. *Combust. Sci. Technol.* 175 (10), 1893–1914.

van Veen, E.H., Roekaerts, D.J.E.M., 2005. Thermometry for turbulent flames by coherent anti-stokes raman spectroscopy with simultaneous referencing to the modeless excitation profile. *Appl. Opt.* 44 (32), 6995–7004.

Veríssimo, A.S., Rocha, A.M.A., Costa, M., 2011. Operational, combustion, and emission characteristics of a small-scale combustor. *Energy Fuels* 25 (6), 2469–2480.

Veríssimo, A.S., Rocha, A.M.A., Costa, M., 2013. Experimental study on the influence of the thermal input on the reaction zone under flameless oxidation conditions. *Fuel Process. Technol.* 106 (0), 423–428.

Weber, R., Smart, J.P., vd Kamp, W., 2005. On the (MILD) combustion of gaseous, liquid and solid fuels in high temperature preheated air. *Proc. Combust. Inst.* 30, 2623–2629.

Widmann, J.F., Presser, C., 2002. *Combust. Flame* 129 (1–2), 47–86.

Wierzba, A., 1990. Deformation and breakup of liquid drops in a gas stream at nearly critical weber numbers. *Exp. Fluids* 9 (1–2), 59–64.

Wood, A.M., Hwang, W., Eaton, J.K., 2005. Preferential concentration of particles in homogeneous and isotropic turbulence. *Int. J. Multiphase Flow* 31 (10–11), 1220–1230.

Wu, S., Chang, W., Chiao, J., 2007. Low NO_x heavy fuel oil combustion with high temperature air. *Fuel* 86 (5–6), 820–828.

Wünning, J.A., Wünning, J.G., 1997. Flameless oxidation to reduce thermal NO_x formation. *Prog. Energy Combust. Sci.* 23, 81–94.

Zoby, M.R.G., Navarro-Martinez, S., Kronenburg, A., Marquis, A.J., 2011. Turbulent mixing in three-dimensional droplet arrays. *Int. J. Heat Fluid Flow* 32 (3), 499–509.